PAPER

The synthesis and characterization of ytterbium-doped TiO₂ hollow spheres with enhanced visible-light photocatalytic activity†

Xueliang Jiang,[ab] Chenjian Li,[b] Song Liu,[b] Fuqing Zhang,[b] Feng You[ab] and Chu Yao [ID] *[ab]

Using $(C_{16}H_{36}O_4)Ti$ and $Yb(NO_3)_3$ solutions as raw materials, Yb-doped TiO_2 hollow spheres (Yb-TiO₂HS) with different doping ratios (Yb : Ti = 0.5%, 1%, and 1.5%) were successfully fabricated *via* a sol–gel template method with melamine–formaldehyde polymer microspheres (MF) as templates. The Yb-TiO₂HS were characterized by scanning electron microscopy, transmission electron microscopy, X-ray diffraction, specific surface area and porosity analysis, ultraviolet-visible-light diffused reflection spectroscopy (UV-DRS), and luminescence spectroscopy. The Yb-TiO₂HS can absorb visible-light and exhibit a lower recombination of electrons (e^-) and holes (h^+) when compared with commercial P25 TiO₂ powder (P25). The photocatalytic activities of the prepared samples were estimated by the degradation process of methyl orange (MO) dye under irradiation with visible-light ($\lambda > 450$ nm). With H_2O_2 and Yb-TiO₂HS (Yb : Ti = 1%) as the promoter and photocatalyst, respectively, the degradation ratio of MO achieved a maximum value (89%) after irradiation for 5 h. While excessive Yb doping resulted in a negative effect on the photocatalysis, an appropriate doping ratio restrained the recombination of electron–hole pairs and extended the light absorption range, thus enhancing the ability of the visible-light photocatalysis. Moreover, the addition of H_2O_2 improved the dye adsorptive activity of TiO₂HS, which further enhanced the photocatalytic effect.

1. Introduction

Dye wastewater, a pollutant of waters from the dyeing and printing industry, is harmful to the environment and human health. Since the components of this pollutant are difficult to degrade under environmental conditions, numerous researchers are concentrated on this issue for effective solutions.

TiO₂ has been extensively applied in the field of water purification and environmental protection due to its high photocatalytic efficiency, chemical and optical stability, low-cost, and non-toxicity.[1–3] However, due to its wide band-gap energy (3.2 eV)[4] and high recombination ratio of electron–hole pairs,[5] only 5% solar-light (ultraviolet) can be absorbed and used by TiO₂. The low absorption of solar light limits the extension of TiO₂ in practical applications. To extend the optical response range and decrease the recombination ratio of electron–hole pairs of TiO₂ and thus obtain effective sunlight or visible-light photocatalytic

[a]Hubei Key Laboratory of Plasma Chemistry and Advanced Materials, China
[b]College of Materials Science and Engineering, Wuhan Institute of Technology, Wuhan 430205, China. E-mail: jiangxl@wit.edu.cn; leechenjian@wit.edu.cn; 201401022@ wit.edu.cn; 04002085@wit.edu.cn; youfeng.mse@wit.edu.cn; chuyao@wit.edu.cn; Tel: +86-27-8719-5661

activity, TiO₂ was modified using some methods such as element doping. Non-metallic (such as B, N, and C) and metallic (such as Fe and Cr) doping can effectively shorten the width of the band gap and inhibit the recombination of photoinduced electron–hole pairs.[6–10]

Due to their incompletely filled 4f and empty 5d orbitals,[11,12] rare earth elements have been widely applied in the fields of up-conversion and luminescence materials,[13,14] catalysis,[15] and solar cells.[16] Doping TiO₂ with rare earth elements not only inhibits the recombination of photoinduced electron–hole pairs in TiO₂ due to the special electron orbit structure of lanthanon, but also restrains the transformation of the anatase phase to the rutile phase in the TiO₂ lattice and crystalline grain thinning.[17–19] Nanostructured Yb³⁺-doped TiO₂ was fabricated by Liu[20] and it displayed improved photocatalysis for the degradation of orangeII. Romero[17] synthesized a series of rare-earth ion-doped TiO₂ powders *via* a sol–gel method and found that the rare earth ions are positive for the photocatalytic performance because they can inhibit the transformation of the crystalline phase of TiO₂ from the anatase to the rutile phase.

Moreover, the photocatalytic activity of TiO₂ is also correlated with its morphology and microstructure. Some special structures such as nanorods,[20] nanotubes,[21] and hollow spheres[22] have been reported to efficiently improve the photocatalytic activity of TiO₂. Among these, hollow spheres have

attracted extensive attention due to their low density and high surface area and thermal stability. Furthermore, the self-light scattering properties of the hollow sphere cavities can improve the availability of sunlight.[10,23–26] Recently, many efforts have been applied in the preparation of nano- or micro-sized hollow spheres. A template-directed synthesis using a hard template, such as carbon or polymer spheres,[27–29] and soft template, such as gas bubbles,[30,31] has been widely applied in the preparation of inorganic hollow spheres due to its higher success rate and facile control of the morphology of the hollow spheres. Melamine–formaldehyde polymer microspheres (MF) have attracted significant attention as a template due to the advantages such as ease of preparation, low-cost, environmentally friendliness, and ease of removal.[32,33]

In this study, Yb-doped TiO_2 hollow spheres (Yb-TiO_2HS) were successfully synthesized via a sol–gel method with the assistance of MF templates. The photocatalytic activities were estimated by the degradation of an aqueous solution of methyl orange (MO) under visible-light irradiation.

2. Experimental

2.1 Preparation of MF

First, 9.8 g formaldehyde solution (37%) and 200 mL deionized water were added into a three-necked flask and heated to 80 °C. Then, 2.5 g melamine was dissolved in the solution under constant stirring for prepolymerization. After 20 min, 0.6 mL of a formic acid (pH = 2) solution was introduced into the aforementioned solution, and the resulting mixture was stirred for 40 min. Finally, white MF were obtained by centrifugation, washing the resulting mixture four times with deionized water, and then drying in air at 60 °C.

2.2 Synthesis of Yb-TiO_2HS

First, 0.2 g of MF was dispersed in 30 mL ethanol (99.9 wt%) by ultrasonication for 30 min in a three-necked flask. Then, 0.05 g of cetyltrimethylammonium bromide (CTAB) was added into the MF dispersion and stirred for 10 min to modify the surface of MF. Next, 0.6027 g of $(C_{16}H_{36}O_4)$Ti (TBOT) was dissolved in 20 mL of ethanol and the resulting solution was added to the MF dispersion. The reaction mixture was heated to 80 °C under magnetic stirring. The $Yb(NO_3)_3$ solution (0.07 mol L^{-1}) with different volumes, corresponding the molar ratios of Yb and Ti (Yb : Ti = 0.5%, 1%, and 1.5%), used as the source of Yb was mixed with 1 mL of deionized water and then added to the reaction system. After stirring at 80 °C for 4 h, the Yb-doped TiO_2@MF composite microspheres (Yb-TiO_2@MFCS) were obtained by centrifugation and washing three times with ethanol and deionized water, and subsequently, drying at 60 °C. The Yb-TiO_2HS samples were obtained after calcining the Yb-TiO_2@-MFCS samples in air at 500 °C for 2 h (ramped up at 4 °C min^{-1}). The obtained samples with different ratios of Yb doping (Yb : Ti = 0.5%, 1%, and 1.5%) were defined as 0.5–1.5%Yb-TiO_2HS. The TiO_2@MF composite microspheres (TiO_2@MFCS) were synthesized using a similar process, and only 1 mL of deionized water was induced into system of the reaction; TiO_2 hollow spheres (TiO_2HS) were prepared using a similar calcination process that was used for the preparation of Yb-TiO_2HS.

2.3 Characterization of Yb-TiO_2HS

The crystal structures of the resulting products were determined using powder X-ray diffraction (XRD, Bruker D8 Advance, Cu-Kα radiation, $\lambda = 0.15418$ nm). Fourier transform infrared spectroscopy (FT-IR) was performed via a PerkinElmer Spectrum Two FT-IR Spectrometer using the potassium bromide (KBr) pellet technique. The morphology and structure of the samples were obtained by scanning electron microscopy (SEM, JSM-5510LV) and transmission electron microscopy (TEM, JEOL, JEM-2100, 200 kV). X-ray photoelectron spectroscopy (XPS) was carried out via a KRATOS AXIS-ULTRA DLD-600 W X-ray photoelectron spectrometer using Al-Kα radiation, and the binding energy reference was taken at 284.6 eV for the C 1s peak. The luminescence spectra were obtained using a fluorescence spectrophotometer (Hitachi, F-4600), with an excitation wavelength of 275 nm. Ultraviolet-visible-light diffused reflection spectra (UV-DRS) were obtained using a PerkinElmer lambda 35 UV/VIS spectrometer with an integration sphere using $BaSO_4$ as the reference sample. Nitrogen (N_2) adsorption–desorption isotherms and pore size distribution curves were obtained at liquid N_2 temperature using a Nova 2000e surface area and pore size analyzer.

2.4 Photocatalytic activity measurements

The photocatalytic performance of Yb-TiO_2HS was estimated by the degradation of a methyl orange (MO) dye solution with a concentration of 20 mg L^{-1} under visible-light irradiation. The photocatalytic reaction device was prepared in the laboratory by our group, as shown in Fig. S1.† A 150 W halogen tungsten lamp was used as the light source. A beaker equipped with a UV cut-off filter cutting the light below 450 nm was used as the photoreactor. In each experiment, 0.05 g of sample was ultrasonically dispersed in 50 mL of the MO solution for 10 s. Then, 5 mL of hydrogen peroxide (H_2O_2), as the promotor, was added to the reaction system under magnetic stirring for 30 min in the dark to achieve an adsorption–desorption equilibrium. Then, the solution was exposed to visible-light irradiation ($\lambda = 450$ nm) in the photoreactor under magnetic stirring. At a given irradiation time interval, 5 mL of the suspension was taken out and centrifuged at 8000 rpm for 10 min to separate the dye solution. The concentration (C) of the centrifuged solution and the initial concentration (C_0) of the MO solution were represented by the absorbance (A_0) and A, respectively, which were obtained using a UV/vis spectrophotometer (PerkinElmer lambda 35 UV/VIS Spectrometer). The degradation rate of MO solution was calculated as $1 - C/C_0$.

3. Results and discussion

3.1 XRD analysis

The XRD patterns of Yb-TiO_2HS with different molar ratios of Yb doping after calcination at 500 °C are shown in Fig. 1. All the samples exhibited typical diffraction peaks according to the standard card data of anatase phase TiO_2 (JCPDS no. 21-1272).
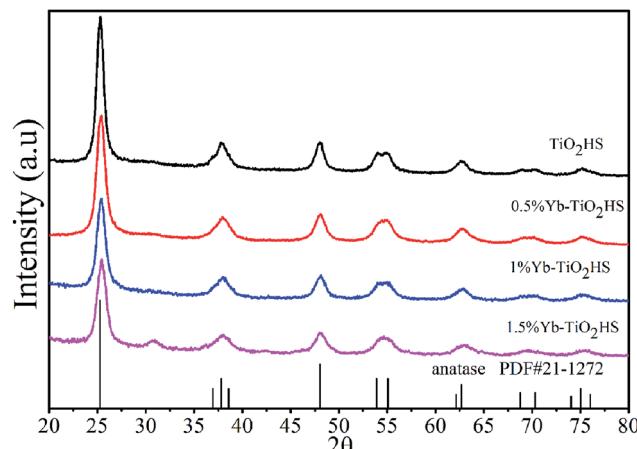
Fig. 1 The XRD patterns of TiO_2HS and Yb-TiO_2HS with different ratios of Yb doping calcined at 500 °C.

No other peaks were observed, except for a weak peak at $2\theta = 30.8°$ corresponding to the brookite plane (121) of the brookite phase TiO_2 in the XRD pattern of 1.5%Yb-TiO_2HS. No ytterbium oxide crystalline phase was found most likely due to the low doping ratios used, which was beyond the detection limitation of XRD. When compared with that of TiO_2HS, the (101) diffraction peak of Yb-TiO_2HS shifted to a high angle region, as shown in Fig. S2.†

The crystalline grain sizes at the anatase diffraction peak (101) were calculated using the Scherrer equation as follows:

$$D = \frac{K\lambda}{B\cos\theta} \tag{1}$$

where D is the crystalline grain size, $\lambda = 0.15418$ nm for Cu Kα radiation, K is a constant usually taken as 0.89, B represents the full width at half maximum (FWHM) of the respective line in radians, and θ is the angle of the Bragg reflection at the anatase diffraction peak (101) of different samples. The crystalline grain sizes decreased after Yb-doping, as shown in Fig. S3.†

The lattice parameters and the unit cell volumes (V) of the unit cell of the anatase phase for both the doped and undoped TiO_2 samples were calculated by the lattice parameter eqn (2) of the tetragonal system and cell volumes formula (3), respectively, The results are presented in Table 1.

$$d_{hkl} = 1 \Big/ \left[\left(h^2 + k^2\right)\Big/a^2 + (1/c)^2 \right]^{1/2} \tag{2}$$

$$V = a^2 c \tag{3}$$

Table 1 The lattice parameters and volume of the unit cell of the samples

Samples	a (Å)	c (Å)	V (Å^3)
TiO_2HS	3.79181	9.50629	136.67975
0.5%Yb-TiO_2HS	3.78068	9.47971	135.49863
1%Yb-TiO_2HS	3.7764	9.45127	134.78642
1.5%Yb-TiO_2HS	3.75132	9.57773	134.78166

As summarized in Table 1, the volume of the unit cell gradually decreased upon increasing the ratio of Yb^{3+} doping.

Because the ionic radius of Yb^{3+} (0.086 nm) is larger than that of Ti^{4+} (0.068 nm), it is more difficult for Yb^{3+} to enter into the TiO_2 lattice. Yb^{3+} is preferentially stacked at the grain boundaries and grain junctions. The crystalline grain sizes of Yb-TiO_2HS are smaller than those of TiO_2HS due to the fact that the doped Yb inhibits the growth of crystalline TiO_2 via the formation of a barrier of Yb–O–Ti bonds.

Fig. 2 shows the XRD patterns of 1%Yb-TiO_2HS and TiO_2HS after calcination at different temperatures. When compared with TiO_2HS, the 1%Yb-TiO_2HS sample after being calcined at 800 °C exhibited all the diffraction peaks belonging to the anatase phase of TiO_2 and the peaks of the rutile phase TiO_2 were absent. This phenomenon indicates that Yb doping effectively prevents the phase conversion of TiO_2 from the anatase to rutile phase.

3.2 FT-IR analysis

Fig. S4† shows the FT-IR spectra of each sample. As shown in the curve of MF, the absorption peaks at 3361 and 2961 cm^{-1} are assigned to the vibration of hydroxy/amino (–OH/–NH–) groups. The peaks at 1558, 1494, and 1353 cm^{-1} are assigned to the vibration of the –NH$_2$ groups and the peaks at 1164, 1007, and 813 cm^{-1} should be attributed to the C–N, C–O–C, and C–N–C vibrations, respectively. These results indicate that the MF resins were successfully synthsized.[33] The FT-IR spectrum of TiO_2@MFCS is similar to that of the MF template, except for a decrease in intensity occurred at some peaks such as the peak corresponding to the ether groups (1007 cm^{-1}). This decrease in the peak intensity can be attributed to the coating of the precursor nanoparticles on the surfaces of the MF. As shown in the spectra of TiO_2HS and 1%Yb-TiO_2HS, the peak at 496 cm^{-1} is the vibrant absorption peak of Ti–O–Ti[34] and the peaks in the range of 3400–3300 cm^{-1} and around 1630 cm^{-1} are the absorption peaks of free –OH in water and adsorbed –OH on the surface of TiO_2.[35] The absorption peaks at 1384 cm^{-1} and 1317 cm^{-1} correspond to the symmetrical vibration of COO–.[36,37] On comparing the spectrum of 1%Yb-TiO_2HS with TiO_2HS, it was observed that the FT-IR spectrum of 1%Yb-TiO_2HS exhibits stronger absorptions corresponding to –OH on the surface of TiO_2 (1636 cm^{-1}). Furthermore, two weak absorption peaks at 1384 cm^{-1} and 1317 cm^{-1} corresponding to COO– were observed after Yb doping. These phenomena indicate that the surface active groups of TiO_2 increased after Yb doping, which is a result of the formation of Lewis acid–base complexes between ytterbium ions containing f-orbitals in the Yb-TiO_2HS and various Lewis bases (such as alcohols, aldehydes, amines, etc.).[38–41]

3.3 XPS analysis

Fig. 3 illustrates the XPS results of the 1%Yb-TiO_2HS after calcination at 500 °C. As shown in Fig. 3a, the peaks at 530.08 eV, 286.08 eV, 185.21 eV, and 458.78 eV corresponding to O 1s, C 1s, Yb 4d, and Ti 2p, respectively, indicate that the product consists of Ti, Yb, O, and C. The C 1s peak at 286.08 eV
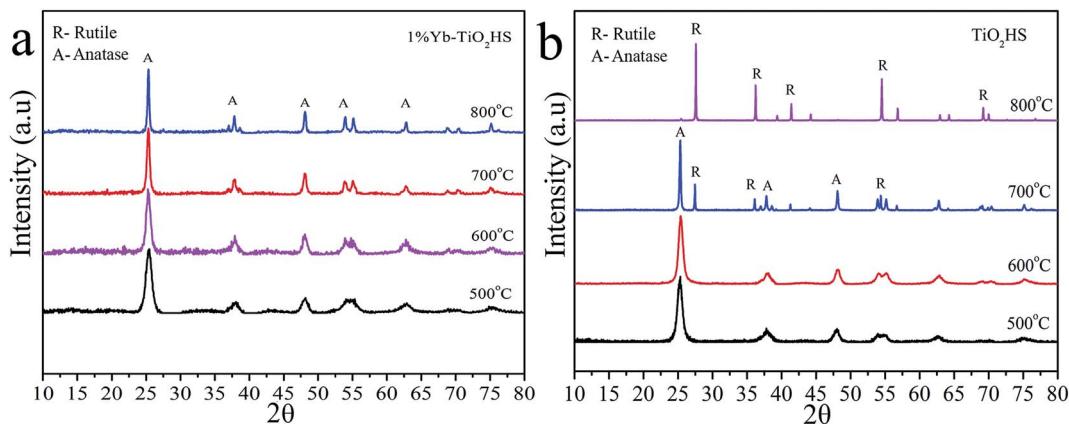
Fig. 2 The XRD patterns of 1%Yb-TiO$_2$HS (a) and TiO$_2$HS (b) after calcination at difference temperatures.

was attributed to residual carbon from the calcined MF and adventitious hydrocarbons from the XPS instrument itself. The high-resolution XPS of Ti 2p is shown in Fig. 3b. The peaks at 458.78 eV and at 464.58 eV are assigned to Ti 2p$_{3/2}$ and Ti 2p$_{1/2}$, respectively, indicating that the main valence of Ti in the obtained sample was +4. Fig. 3c presents the high-resolution XPS of Yb 4d. The peaks of Yb 4d$_{5/2}$ at 185.21 eV and Yb 4d$_{3/2}$ at 194.72 eV prove the existence of Yb^{3+}. As shown in Fig. 3d, three second splits of the O 1s peaks at 530.05 eV, 530.48 eV, and 531.98 eV are assigned as the bonding energies for the TiO$_x$, Ti–OH, and C–OH bonds, respectively.[42]

3.4 Morphology, specific surface area, and porosity analysis

The TEM and the SEM images indicate that each sample has a uniform spherical morphology with a size about 1.8–2 μm. The SEM images of the MF with smooth surfaces are shown in Fig. 4a. As shown in Fig. 4b, the TiO$_2$@MFCS inherit the spherical morphology of the MF templates, but the surface of the composite microspheres are much rougher than those of pure MF due to the TBOT hydrolysis reaction, which generated the MF templates coated with the TiO$_2$ colossal particles; thus, the size of the TiO$_2$@MFCS (about 2 μm) became slightly larger than that of MF (about 1.8 μm) (Fig. 4b). Fig. 4c, d and e, f show
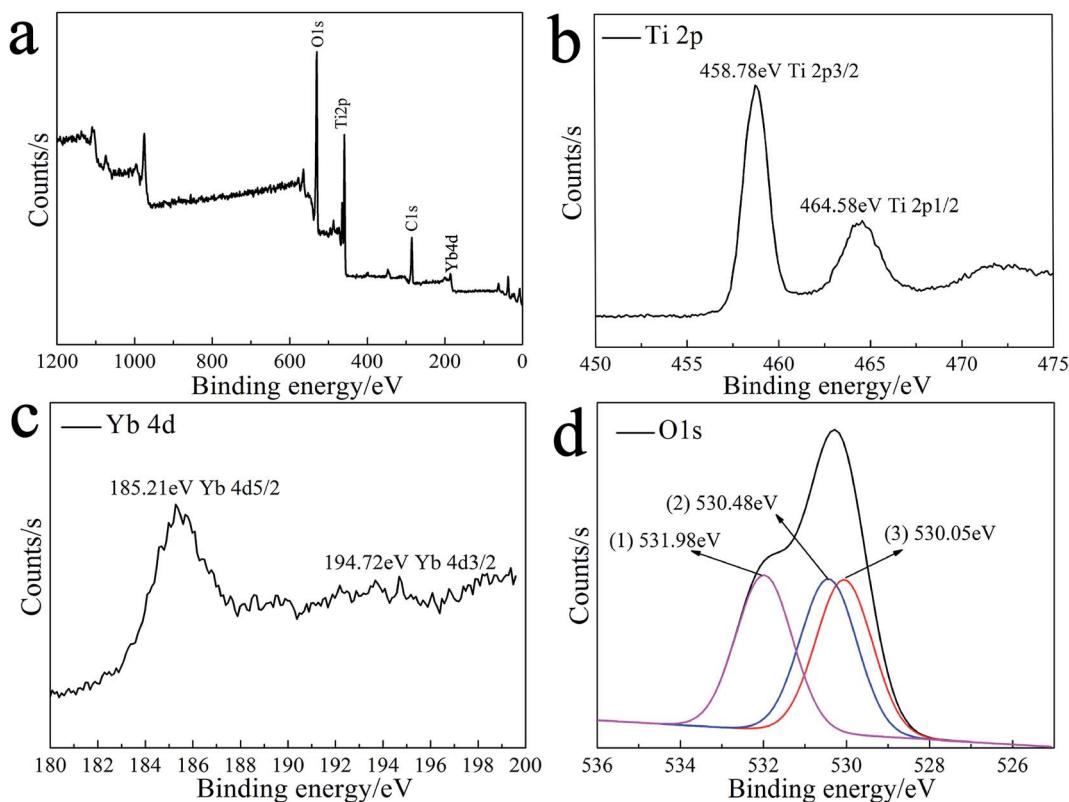

Fig. 3 The XPS spectra of 1%Yb-TiO$_2$HS: the general XPS survey spectrum (a) and Ti 2p (b), Yb 4d (c) and O 1s (d) spectra.

the SEM images of TiO$_2$HS and 1%Yb-TiO$_2$HS, respectively. The crushed microspheres shown in Fig. 4c and e revealed that the microspheres are hollow structures. The obtained microspheres have an average particle size of about 1.8 μm. As shown in the TEM images of 1%Yb-TiO$_2$HS (Fig. 5), the strong contrast between the dark edges and the pale center further confirms that all the microspheres have a large hollow cavity of about 1.8 μm size, which is in agreement with the TEM observations. Overall, the 1%Yb-TiO$_2$HS was successfully fabricated by a sol–gel template method using the MF as the template.

The N$_2$ adsorption–desorption curves of 1%Yb-TiO$_2$HS and TiO$_2$HS are shown in Fig. S5a and b,† respectively; the curves exhibit isotherms with a clear hysteresis loop, indicating the existence of mesoporous structures of 1%Yb-TiO$_2$HS and TiO$_2$HS. The specific surface areas of 1%Yb-TiO$_2$HS and
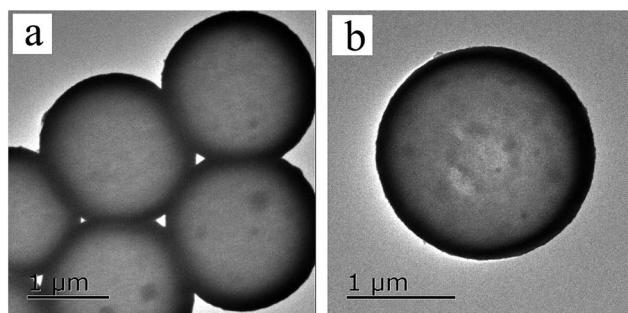
Fig. 5 TEM image of 1%Yb-TiO$_2$HS.
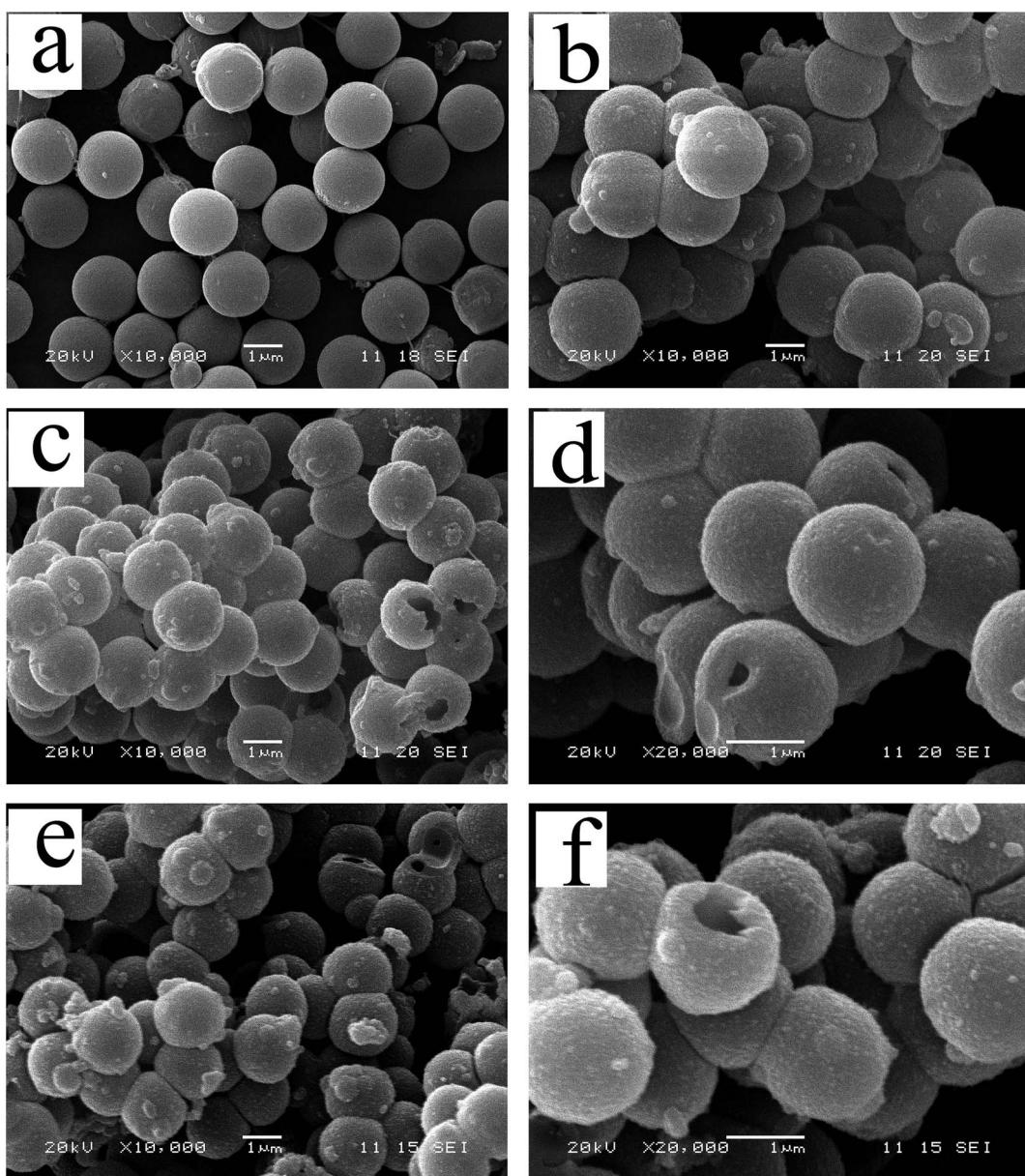
Fig. 4 SEM image of MF (a), TiO$_2$@MFCS (b), TiO$_2$HS (c and d) and 1%Yb-TiO$_2$HS (e and f).

Table 2 The E_g value of the samples

Sample	P25	TiO$_2$HS	0.5%Yb-TiO$_2$HS	1%Yb-TiO$_2$HS	1.5%Yb-TiO$_2$HS
E_g/eV	3.04	2.98	2.93	2.95	2.94

TiO$_2$HS, determined by the Brunauer–Emmett–Teller method, are 64.655 m^2 g^{-1} and 23.814 m^2 g^{-1}, respectively. This indicates that Yb doping can increase the surface area to some extent. The pore size distribution curves of 1%Yb-TiO$_2$HS and TiO$_2$HS, shown in Fig. S5c and d,† were calculated from the desorption branch obtained by Barrett–Joyner–Halenda method. In both cases, the most abundant peaks appeared at around 5 nm, indicating that most of the pores in 1%Yb-TiO$_2$HS and TiO$_2$HS have a size of 5 nm. The abovementioned results confirmed the mesoporous structures of 1%Yb-TiO$_2$HS and TiO$_2$HS.

3.5 Luminescence and UV-vis diffuse reflection spectrum (UV-DRS)

The optical absorption abilities of the samples were demonstrated by diffuse reflectance spectroscopy (DRS) in the optical wavelength range of 300–800 nm, as shown in Fig. S6.† When compared with commercial P25 TiO$_2$ powder (P25), the absorption peaks of TiO$_2$HS and Yb-TiO$_2$HS exhibit a significant enhancement in intensity in the region of visible-light. The K–M function transformed spectra of the samples were obtained using the Kubelka–Munk function method (K–M function),[43] as shown in Fig. S7.†

The corresponding values of the band gap (E_g) were calculated according to tangent valuation method, as shown in Table 2. Upon Yb doping, the E_g value gradually decreased.

Although the electrons (e$^-$) and holes (h$^+$) separate under light irradiation (λ_{ex} = 275 nm), the e$^-$ and h$^+$ combined, generating a luminescence phenomenon. The intensity of the luminescence reflects the recombination ratio of the e$^-$ and h$^+$. The shapes of the luminescence spectra of each sample are

quite similar, as shown in Fig. S8.† The lowest intensity of 1% Yb-TiO$_2$HS indicates the lowest recombination ratio of the e$^-$ and h$^+$.

3.6 Visible-light photocatalytic activity

The visible-light (λ > 450 nm) photocatalytic activities of the samples were estimated using degradation of MO dye, as shown in Fig. 6a. The photocatalytic activity of TiO$_2$HS is better than that of P25. Upon Yb doping, the photocatalytic activity of the Yb-TiO$_2$HS is further improved and reaches a maximum of 89% MO degradation at the doping ratio of 1%. Fig. 6b shows that the MO was almost completely degraded with 1%Yb-TiO$_2$HS after 5 h. Since excessive Yb will form a new center for the recombination of electron–hole pairs, the photocatalytic activity will decrease if the doping ratio of Yb is significantly increased. Fig. S9† shows the cyclic activity of 1%Yb-TiO$_2$HS under visible-light irradiation. After three cycles, the degradation of MO remained at 89%.

Fig. 7a and b show the photocatalytic decomposition rates and the surface absorption abilities of the MO solution at pH of 1, 3, 5, 7, and 9 with 1%Yb-TiO$_2$HS, respectively. Upon increasing the pH, the decomposition rate and the surface absorption ability decreased. These results prove that the positive surface charge of TiO$_2$ under an acid environment is beneficial for TiO$_2$ to absorb the anionic MO and the enhancement of its photocatalysis ability.[27] As shown in Fig. 7c, the effect of photocatalysis without H$_2$O$_2$ is lower than that with H$_2$O$_2$. H$_2$O$_2$ can provide not only O$_2$ and OH$^-$, but also H$^+$ to increase the acidity of the reaction system, which can improve the photocatalytic effect.

3.7 Mechanism for the enhanced visible-light photocatalytic activity of Yb-TiO$_2$HS

Extending the light absorption of TiO$_2$ to the visible region and narrowing the band gap of TiO$_2$ are effective methods for enhancing visible-light photocatalytic activity. As mentioned in the UV-DRS analysis (Fig. S6†) and the data obtained for the band gaps (Table 2), Yb-TiO$_2$HS exhibited a wider absorption range in the visible region and a narrower band gap than pristine TiO$_2$. These results were attributed to two reasons, as shown in Scheme 1. The first reason is the band gap narrowing,
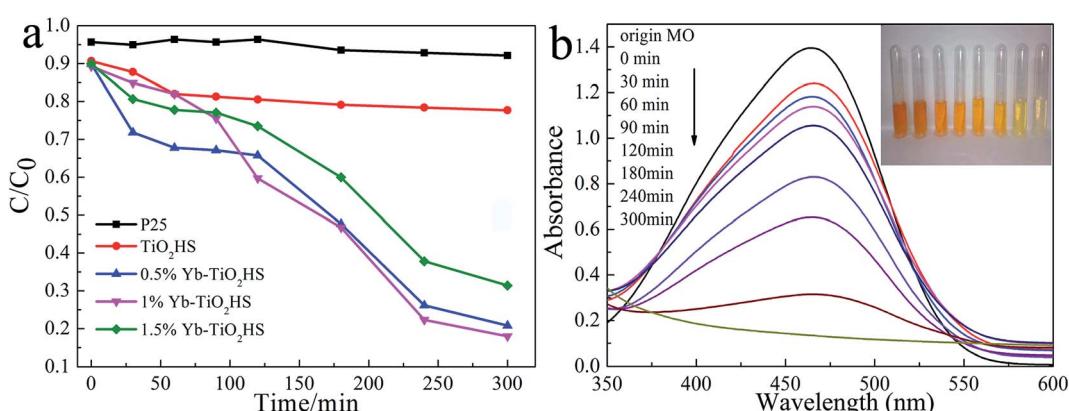

Fig. 6 A comparison of the photodegradation rates of MO with H$_2$O$_2$ addition obtained for the different samples (a) and the absorbance and resulting pictures of MO upon photodegradation with 1%Yb-TiO$_2$HS at difference times (b).
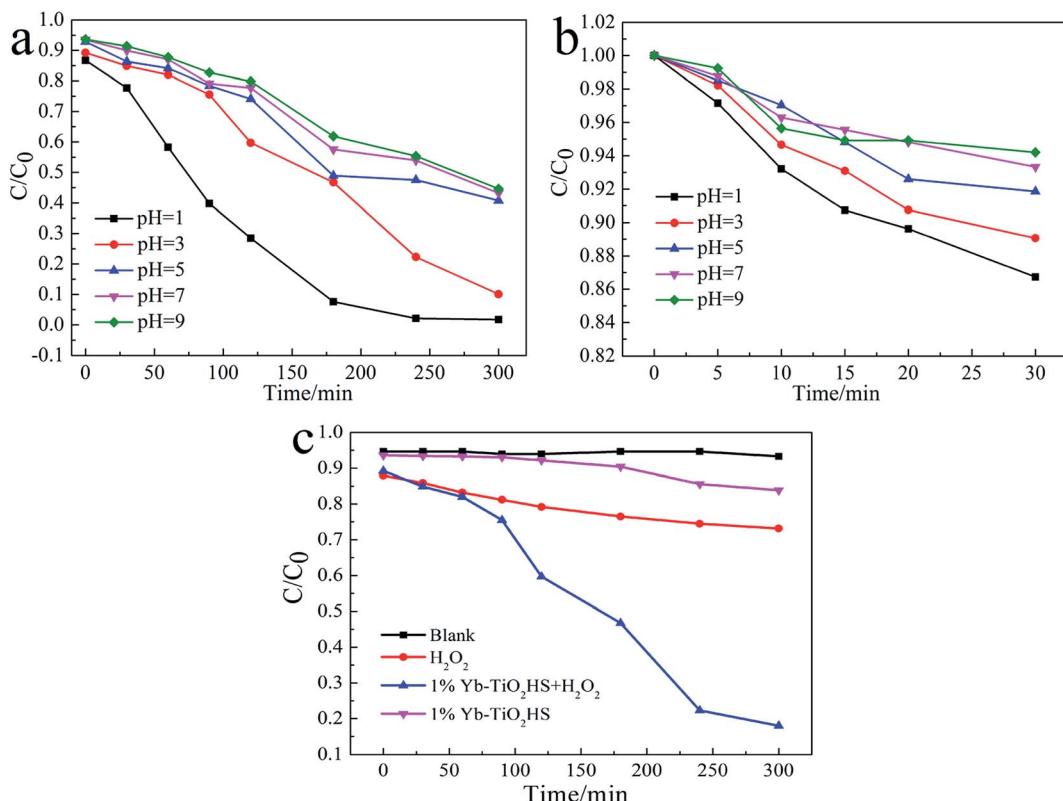
Fig. 7 The photocatalytic decomposition rates (a), surface absorption abilities of the MO solution at different pH values with 1%Yb-TiO_2HS (b) and the effects of H_2O_2 on MO degradation (c).

in which Yb doping leads to the appearance of oxygen vacancy defects.[44] In addition, a small amount of residual carbon atom doping in TiO_2 replaced the oxygen state in the TiO_2HS lattice *via* the calcination of MF at 500 °C, which also leads to a narrowing of the band gap.[45]
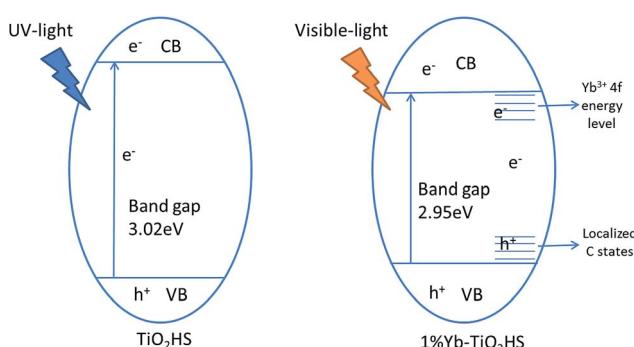
The second reason is the separation of electron–hole pairs; the luminescence spectra (Fig. S8†) indicates that Yb^{3+} doped in TiO_2 can form centres for electron capture, promoting the separation of the electron–hole pairs. The reason for this was attributed to the formation of an empty 4f impurity energy level in the rare earth ions between the conduction and valence bands in the TiO_2 energy band structure.[44,46,47] However, the luminescence intensity of 1.5%Yb-TiO_2HS was stronger than that of 1%Yb-TiO_2HS, which

shows that an excessive Yb^{3+} in TiO_2 will form a new center for the recombination of the e^- and h^+.
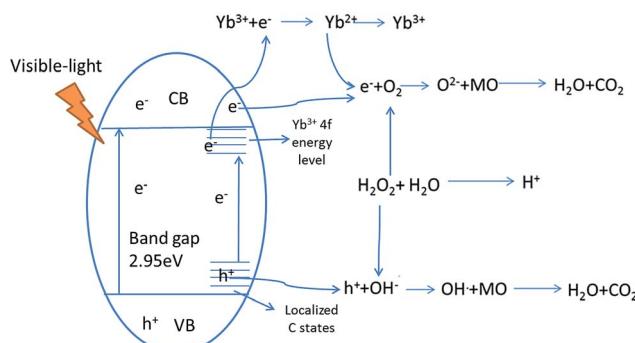
The XPS (Fig. 3d) and the FT-IR (Fig. S4†) spectra show species such as –OH and COO– on the surface of TiO_2 after Yb doping. These species can promote the degradation of dye under light irradiation. Moreover, Yb doped in TiO_2 can restrain the phase transition of TiO_2 from anatase to rutile (Fig. 2). The crystalline grain sizes of Yb-TiO_2HS (Fig. S3†) calculated using the Scherrer equation indicate that a certain ratio of Yb dopant can lead to crystalline grain size thinning. The small crystalline grain size can increase the surface area of TiO_2HS, which was proven in the BET analysis (Fig. S5†).

### 3.8 The mechanism of the visible-light photocatalytic reaction of Yb-TiO_2HS

The photocatalytic process of Yb-TiO_2HS is shown in Scheme 2. H_2O_2 can form O_2, OH^-, and H^+ upon light irradiation, electron (e^-)–hole (h^+) pairs can be generated at the valence band after visible-light irradiation, and the e^- can be captured by the 4f impurity energy level of Yb^{3+} or cross the band gap to transfer to the conduction band. After transferring to the conduction band or being captured by the 4f energy level of Yb^{3+}, the e^- can react with O_2 to produce the O^{2-}. Moreover, the h^+ at the valence band and localized C state will react with OH^- formed from the decomposition of H_2O_2 to produce the $OH^{\cdot}$.[10] O^{2-} and $OH^{\cdot}$ can oxidize MO to CO_2 and H_2O.[48–50] In addition, the acidic environment prompts the photodegradation of MO under visible-

Scheme 1 The energy band structures of TiO_2HS and 1%Yb-TiO_2HS.

Scheme 2 The photocatalytic processes of Yb-TiO$_2$HS.

light irradiation, and the decomposition of H$_2$O$_2$ can provide a certain amount of H$^+$.

4. Conclusions

In summary, Yb-doped TiO$_2$ hollow spheres (Yb-TiO$_2$HS) and TiO$_2$ hollow spheres (TiO$_2$HS) were successfully prepared *via* a sol–gel template method using melamine–formaldehyde polymer microspheres (MF) as the template. When compared with P25 TiO$_2$ powder (P25), Yb-TiO$_2$HS exhibited an enhanced absorption in the visible region and a lower recombination of electron–hole pairs. The photocatalytic activities of Yb-TiO$_2$HS, TiO$_2$HS, and P25 under visible-light irradiation were estimated using the photocatalytic degradation of MO dye. Yb-TiO$_2$HS and the TiO$_2$HS show better photocatalytic activities than P25, indicating that Yb doping and the hollow sphere structure can enhance the photocatalytic activity of TiO$_2$ under visible-light irradiation. In addition, H$_2$O$_2$ plays a crucial role as a promotor, providing O$_2$, OH$^-$, and H$^+$ to the photocatalytic reaction system, thus promoting the photodegradation effect of Yb-TiO$_2$HS.

Acknowledgements

References

1 K. Sridharan, E. Jang and T. J. Park, *Appl. Catal., B*, 2013, **142–143**, 718–728.

2 J. Santiago-Morales, A. Agüera, M. D. M. Gómez, A. R. Fernández-Alba, J. Giménez, S. Esplugas and R. Rosal, *Appl. Catal., B*, 2013, **129**, 13–29.

3 D. Dolat, S. Mozia, B. Ohtani and A. W. Morawski, *Chem. Eng. J.*, 2013, **225**, 358–364.

4 C. Ye, B. Tian and J. Zhang, *Appl. Catal., B*, 2011, **101**, 376–381.

5 N. Aman, P. K. Satapathy, T. Mishra, M. Mahato and N. N. Das, *Mater. Res. Bull.*, 2012, **47**, 179–183.

6 C. L. Muhich, J. Y. Westcott, T. Fuerst, A. W. Weimer and C. B. Musgrave, *J. Phys. Chem. C*, 2014, **118**, 27415–27427.

7 X. Fan, X. Chen, S. Zhu, Z. Li, T. Yu, J. Ye and Z. Zou, *J. Mol. Catal. A: Chem.*, 2008, **284**, 155–160.

8 C. Xu, A. Cui, Y. Yuan, Z. Chen, R. Yuan and X. Fu, *J. Mater. Sci.*, 2013, **48**, 3428–3435.

9 H. Li, Y. Hao, H. Lu, L. Liang, Y. Wang, J. Qiu, X. Shi, Y. Wang and J. Yao, *Appl. Surf. Sci.*, 2015, **344**, 112–118.

10 J. W. Shi, X. Zong, X. Wu, H. J. Cui, B. Xu, L. Wang and M. L. Fu, *ChemCatChem*, 2012, **4**, 488–491.

11 L. Zhang, J. Luo, M. Wu, H. Jiu and Q. Chen, *Mater. Lett.*, 2007, **61**, 4452–4455.

12 N. Aman, P. K. Satapathy, T. Mishra, M. Mahato and N. N. Das, *Mater. Res. Bull.*, 2011, **47**, 179–183.

13 J. Wang and P. A. Tanner, *J. Am. Chem. Soc.*, 2009, **132**, 947–949.

14 H. Jiu, Y. Fu, L. Zhang and Y. Sun, *Micro Nano Lett.*, 2012, **7**, 287–291.

15 J. Zhou, L. Xu, J. Sun, D. He and H. Jiao, *Surf. Coat. Technol.*, 2015, **271**, 119–126.

16 T. Liu, X. Bai, C. Miao, Q. Dai, W. Xu, Y. Yu, Q. Chen and H. Song, *J. Phys. Chem. C*, 2014, **118**, 3258–3265.

17 D. D. L. C. Romero, G. T. Torres, J. C. Arévalo, R. Gomez and A. Aguilar-Elguezabal, *J. Sol-Gel Sci. Technol.*, 2010, **56**, 219–226.

18 M. Borlaf, M. T. Colomer, R. Moreno and A. L. Ortiz, *J. Am. Ceram. Soc.*, 2014, **34**, 4457–4462.

19 L. Cheng, X. Xu, Y. Fang, Y. Li, J. Wang, G. Wan, X. Ge, L. Yuan, K. Zhang and L. Liao, *Sci. China: Chem.*, 2015, **58**, 850–857.

20 Y. Liu, *Nanoscale*, 2016, **8**, 46–54.

21 Y. Lv, Z. Xu, H. Asai, N. Shimada and K. Nakane, *RSC Adv.*, 2016, **6**, 21043–21047.

22 X. Lin, D. Fu, L. Hao and D. Zhen, *J. Environ. Sci.*, 2013, **25**, 2150–2156.

23 Z. Q. Li, Y. P. Que, L. E. Mo, W. C. Chen, Y. Ding, Y. M. Ma, L. Jiang, L. H. Hu and S. Y. Dai, *ACS Appl. Mater. Interfaces*, 2015, **7**, 10928–10934.

24 P. Liu, Y. Li, Y. Hu, X. Hou and C. Li, *Ind. Eng. Chem. Res.*, 2015, **54**, 6692–6697.

25 J. W. Shi, H. J. Cui, X. Zong, S. Chen, J. Chen, B. Xu, W. Yang, L. Wang and M. L. Fu, *Appl. Catal., A*, 2012, **435–436**, 86–92.

26 M. L. Sang, K. H. Park and S. C. Hong, *Chem. Eng. J.*, 2012, **195–196**, 323–331.

27 X. Qu, X. Yan, Y. Hou, P. Wang, H. Song and F. Du, *J. Sol-Gel Sci. Technol.*, 2015, **76**, 699–707.

28 J. Zhang, L. Li, Z. Xiao, D. Liu, S. Wang, J. Zhang, Y. Hao and W. Zhang, *ACS Sustainable Chem. Eng.*, 2016, **4**, 2037–2046.

29 X. Jiang, L. Yu, C. Yao, F. Zhang, J. Zhang and C. Li, *Materials*, 2016, **9**, 323.

30 Y. Y. Wang, G. Q. Zhou, J. Guo and T. Q. Liu, *Ceram. Int.*, 2016, **42**, 12467–12474.

31 M. Mozafari, F. Moztarzadeh, A. M. Seifalian and L. Tayebi, *J. Lumin.*, 2013, **133**, 188–193.

32 S. Gai, L. Wang, M. Zhang, S. Huang and P. Yang, *Inorg. Chem.*, 2013, **52**, 9184–9191.

33 Y. Wu, Y. Li, L. Qin, F. Yang and D. Wu, *J. Mater. Chem. B*, 2012, **1**, 204–212.

34 C. Song, W. Yu, B. Zhao, H. Zhang, C. Tang, K. Sun, X. Wu, L. Dong and Y. Chen, *Catal. Commun.*, 2009, **10**, 650–654.

35 Y. S. Li, F. L. Jiang, Q. Xiao, R. Li, K. Li, M. F. Zhang, A. Q. Zhang, S. F. Sun and Y. Liu, *Appl. Catal., B*, 2010, **101**, 118–129.

36 C. P. Sibu, S. R. Kumar, A. P. Mukundan and K. G. K. Warrier, *Chem. Mater.*, 2002, **14**, 2876–2881.

37 A. D. Weisz, L. G. A. Rodenas, P. J. Morando, A. E. Regazzoni and M. A. Blesa, *Catal. Today*, 2002, **76**, 103–112.

38 P. Ji, M. Takeuchi, T. M. Cuong, J. Zhang, M. Matsuoka and M. Anpo, *Res. Chem. Intermed.*, 2010, **36**, 327–347.

39 K. T. Ranjit, I. Willner, A. S. H. Bossmann and A. M. Braun, *Environ. Sci. Technol.*, 2001, **35**, 1544–1549.

40 T. D. Nguyen-Phan, M. B. Song, E. J. Kim and E. W. Shin, *Microporous Mesoporous Mater.*, 2009, **119**, 290–298.

41 H. Shi, T. Zhang, T. An, B. Li and X. Wang, *J. Colloid Interface Sci.*, 2012, **380**, 121–127.

42 A. Rjeb, S. Letarte, L. Tajounte, M. C. E. Idrissi, A. Adnot, D. Roy, Y. Claire and J. Kaloustian, *J. Electron Spectrosc. Relat. Phenom.*, 2000, **107**, 221–230.

43 D. Reyes-Coronado, G. Rodríguez-Gattorno, M. E. Espinosa-Pesqueira, C. Cab, C. R. De and G. Oskam, *Nanotechnology*, 2008, **19**, 145605.

44 P. Yan, H. Jiang, S. Zang, J. Li, Q. Wang and Q. Wang, *Mater. Chem. Phys.*, 2013, **139**, 1014–1022.

45 Z. Ying, Z. Zhao, J. Chen, C. Li, J. Chang, W. Sheng, C. Hu and S. Cao, *Appl. Catal., B*, 2015, **165**, 715–722.

46 J. Castañeda-Contreras, V. F. Marañón-Ruiz, R. Chiu-Zárate, P. L. D. Guevara, R. Rodriguez and C. Michel-Uribe, *Mater. Res. Bull.*, 2012, **47**, 290–295.

47 J. Reszczyńska, T. Grzyb, J. W. Sobczak, W. Lisowski, M. Gazda, B. Ohtani and A. Zaleska, *Appl. Catal., B*, 2014, **163**, 40–49.

48 Y. Shen, W. Wang and K. Xiao, *J. Environ. Chem. Eng.*, 2016, **4**, 1259–1266.

49 Y. Jiang, W. N. Wang, P. Biswas and J. D. Fortner, *ACS Appl. Mater. Interfaces*, 2014, **6**, 303–313.

50 R. Palominos, J. Freer, M. A. Mondaca and H. D. Mansilla, *J. Photochem. Photobiol., A*, 2008, **193**, 139–145.